REVIEW OF AERONAUTICAL FATIGUE INVESTIGATIONS IN JAPAN DURING THE PERIOD JUNE 2023 TO MAY 2025

Edited by

Takao Okada
Japan Aerospace Exploration Agency

For Presentation at the 39th Conference of
the International Committee on Aeronautical Fatigue and Structural Integrity

Xi'an, China, 9-13 June, 2025

CONTENTS

5. MISCELLANEOUS

1. INTRODUCTION

Takao Okada, Japan Aerospace Exploration Agency

This review summarizes the papers on the study of aeronautical fatigue, structural integrity and related themes conducted in Japan during June 2023 to May 2025.

The papers were contributed by following organizations:

Japan Aerospace Exploration Agency (JAXA)
Japan Transport Safety Board (JTSB)
Kyushu University
Shibaura Institute of Technology, Tokyo, Japan
Shoden Corporation
Tokyo University of Agriculture and Technology
The University of Tokyo
Waseda University

The general activities on aircraft development program in Japan during 2023 to 2025 is summarized as follows:

- JAXA establishes the consortium named Comprehensive Aviation Innovation by digital transformation (CHAIN-X) at June 17 in 2022, in order to increase an aviation industry in Japan, enhance its international competitiveness and develop a human resource work at digital transformation (DX) in aviation industry. Ministry of economy, trade and industry and 11 related organizations participate in CHAIN-X. CHAIN-X acts as central role for research and development in the field of optimization and acceleration using DX in design, certification, manufacturing, operation and recycle of aircraft. As of April 2025, 69 organizations participate in the consortium.

- Ministry of land, infrastructure and transport and Ministry of economy, trade and industry jointly organize a council to discuss emerging technology for de-carbonization in aviation. Public and Private sector are involved in the council and working group for motorization, hydrogen powered and weight reduction are established. Four meetings have been held so far.

- The WEATHER (Weather Endurance Aircraft Technology to Hold, Evade and Recover) -Eye consortium is established in 2016, in order to improve the operational safety and efficiency under the severe weather condition such as slippery short runway, severe lightning, crystal ice drop and volcanic ash. From the material point of view, development of the CFRP with high conductivity through the thickness direction using conductive polymer have been conducted to reduce the lightning damage. Hight conductive polymer using polyaniline (PANI) is developed and the reduction of the lightning damage using the polymer is demonstrated. The modification of the polymer is underway. As of April 2025, 55 organizations participate in the consortium.

2 FATIGUE AND FAILURE IN METALLIC MATERIALS AND COMPONENTS

2.1 Effect of temperature on tensile and fatigue properties of additively manufactured AlSi10Mg lattice structure

Shiyu Suzuki[1], Natsuki Tsushima[1,2,3]

1Japan Aerospace Exploration Agency (JAXA), Tokyo, Japan

2Kyushu University, Fukuoka, Japan

3The University of Tokyo, Tokyo, Japan

An additively manufactured (AM) aluminum alloy, AlSi10Mg, is one of the most widely used AM alloys in aerospace and automotive industries thanks to its excellent property of the strength-to-weight ratio. The alloy's lightweight performance has been often enhanced via utilizing lattice structures which consist of unit cells comprised of struts or thin planes. Numerous works have been performed to examine mechanical properties such as tensile/compressive and fatigue properties of the AlSi10Mg lattice structures. However, most of the previous works have investigated the mechanical performance at room temperature (RT), and the understanding of an effect of the temperature has been limited. This study investigated the effect of the temperature on the tensile and fatigue properties of an AM AlSi10Mg lattice structure from -60 °C to 200 °C.

A laser powder bed fusion (L-PBF) machine, EOS M 290, was used to manufacture specimens for mechanical tests. Two types of specimens were used in this study: a cylindrical specimen for the standard fatigue test of the bulk material (Fig.2.1.1(a)) and a lattice specimen for tensile and fatigue tests of the lattice structure (Fig.2.1.1(b)). The lattice specimen is composed of simple cubic unit cells (UCs) whose size was 3 mm × 3 mm × 3 mm with a struts' width of 0.5 mm. The mass ratio of the UC to the bulk material was 0.26. The gauge section of the lattice specimen was composed of 6 UCs along the loading direction and 10 UCs along directions normal to the loading direction. Also, there are complementary three layers of the UCs with gradient strut widths between the gauge section and the bulk material (grip section) to reduce stress concentration. All the specimens were manufactured on the same build platform and were built along the vertical direction.

Three lattice specimens were tested in static tensile tests at RT, -60 °C and 200 °C, and seven lattice specimens were tested in fatigue tests at RT and 200 °C under load-controlled conditions. A servo-hydraulic testing machine with an environmental chamber was used. For the fatigue tests, a loading frequency was 10 Hz, and a load ratio R was 0.1. The test set-up of the lattice specimen is shown in Fig.2.1.1(c). Also, three cylindrical specimens were tested in fatigue tests at RT under the same load-controlled conditions as the lattice specimens.

Fig.2.1.1(d) shows load-displacement curves obtained by the static tensile tests using the lattice specimens at RT, -60 °C and 200 °C. At RT, the maximum load and displacement values were about 26 kN and 0.5 mm, respectively. At -60 °C, the maximum load value increased to about 28 kN whereas the maximum displacement remained the equivalent value, 0.5 mm. At 200 °C, the maximum load value decreased to about

15 kN whereas the maximum displacement increased to 1.7 mm. In summary, as the temperature increases, the strength of the lattice structure decreases whereas the ductility increases.

Fig.2.1.1(e) shows a S-N diagram obtained by all the fatigue tests using the lattice and cylindrical specimens. For the tests using the lattice specimens at RT, the load-displacement curves during the tests were confirmed to be almost completely linear without hysteresis areas, indicating that the deformations in these tests were elastic-dominant (so-called “high cycle fatigue”). Thus, Basquin’s law that is often used to the high cycle fatigue life was applied to these tests, which exhibits a good correlation between the fitted curve and the experimental results. Also, when compared to the cylindrical specimens at RT, the lattice specimens show significantly shorter fatigue lives that are less than one-tenth of those of the cylindrical specimens under the same stress values. Based on observations of the fractured lattice specimens, the struts in the UCs were found to be fractured at intersections with other struts probably due to the stress concentrations. The shorter fatigue lives of the lattice specimens than the cylindrical specimens are possibly because of the existence of these stress concentrations in the lattice structure.

For the tests using the lattice specimens at 200 °C, although the load-displacement curves during the tests were almost elastic-dominant, observations of the fractured specimens found an evident appearance of permanent inelastic deformation only under the highest stress condition, i.e., a stress amplitude, σ_{amp} = 50.8 MPa. Thus, it can be speculated that the test at σ_{amp} = 50.8 MPa was so-called “low cycle fatigue” whereas the other tests under lower stress conditions ($\sigma_{amp} \leq$ 40.9 MPa) were the high cycle fatigue. When compared to RT, the fatigue tests at 200 °C show a significantly shorter fatigue life in the low cycle fatigue regime (σ_{amp} = 50.8 MPa). This is reasonable considering that the strength of the lattice specimen at 200 °C was significantly lower than that at RT (Fig.2.1.1(d)). On the other hand, the fatigue tests at 200 °C show equivalent or slightly longer fatigue lives compared to RT in the high cycle fatigue regime ($\sigma_{amp} \leq$ 40.9 MPa). This is surprising considering the temperature dependence of the tensile strength mentioned above. Also, in the literature, the fatigue life of the AM AlSi10Mg has been reported to decrease with increasing temperatures using bulk specimens [1]. Thus, the longer fatigue lives at 200 °C than at RT may be a unique characteristic of the lattice structure.

In conclusion, this study investigated the static tensile and fatigue properties of the AM AlSi10Mg lattice structure at RT, -60 °C and 200 °C. In the static tensile tests, as the temperature increased, the strength decreased whereas the ductility increased. In the fatigue tests, all the lattice specimens tested at RT showed the high cycle fatigue behavior with the elastic-dominant deformation, and Basquin’s law was successfully applied to evaluate the experimental fatigue lives. The lattice specimens showed significantly shorter fatigue lives than the cylindrical specimens possibly because of the existence of these stress concentrations in the lattice structure. At 200 °C, the lattice specimens showed a shorter fatigue life than at RT in the low cycle fatigue regime whereas longer fatigue lives than at RT in the high cycle fatigue regime. The longer fatigue lives at 200 °C than at RT may be a unique characteristic of the lattice structure. In summary, to properly evaluate and predict the fatigue life of the lattice structure at different temperatures, it is necessary to consider geometric and structural features such as stress concentration sites specific to the lattice structure.

References

[1] Wang, Z., Wu, W., Qian, G., Sun, L., Li, X., Correia, JAFO., 2019. In-situ SEM investigation on fatigue behaviors of additive manufactured Al-Si10-Mg alloy at elevated temperature. Engineering Fracture Mechanics 214, 149–163.

2.2 Investigation of strength demonstration test for materials

Seiichi Ito[1], Hisaya Katoh[1] and Takao Okada[1]

1Japan Aerospace Exploration Agency (JAXA), Tokyo, Japan

The lower bounds used in the binary evaluation based on the reliability R and the confidence level 1-g defined in MIL standards are set to be highly conservative. Therefore, depending on the intended application, they may not appropriately reflect actual conditions. In this study, we apply the interval estimation theory proposed by Meeker et al. (2017) and design appropriate sampling plans by first setting a target demonstrated probability, which is then statistically verified. Let F_{xL} denote the probability distribution of the one-sided tolerance limit x_L, defined under the MIL standard for a given sample size n. The demonstrated probability is defined as: $R_{demo}(x_L^*) = 1\text{-}F_{xL}(x_L^*)$ where x_L^* is referred to as the demonstrated lower bound. For example, if the demonstrated probability is set to $R_{demo}(x_L^*) = 0.9$, and the lower bound x_L obtained from experimental results is greater than or equal to x_L^*, then the strength demonstration test is considered to have a 90% probability of success at the confidence level 1-g. Conversely, if x_L is below x_L^*, the estimate is overly conservative, and redesigning the sampling plan may be necessary. Let the true cumulative distribution function of strength x be denoted by $F_{true}(x)(R_{true}(x)\text{-}1)$. In this context, $R_{true}(x_L^*)$ serves as a criterion for evaluating whether the estimated reliability is overly conservative (Figure 2.2.1).

When the strength distribution is assumed to follow a normal distribution, the exact form of the distribution F_{xL} can be derived. However, for other distributions, such closed-form solutions are not available, and the lower bounds and their associated true reliabilities must be estimated using Monte Carlo (MC) simulations. As a case study, we consider the calculation of the strength demonstration probability of a two-parameter Weibull distribution W(x|a,b) using Type II censored samples obtained by assuming the true values. After transforming the variables to the extreme value domain, we estimate the Weibull parameters via maximum likelihood estimation (MLE), and similarly to the normal distribution, compute the coefficient of variation for interval estimation. Subsequently, MC simulations are performed to evaluate the lower bounds. Under the MIL-B conditions of a target reliability R = 0.9 and confidence level 1-g = 0.95, the simulation provides empirical distributions of both the actual reliability and the lower bound (Figure 2.2.2). For a fixed sample size of n = 100, and varying numbers of censored failures r = 6,10,30, 50,100, if the actual reliability is set to $R_{true}(x_L^*) = 0.96$, the demonstrated probability R_{demo} increases as r increases. For instance, when r = 50, the demonstrated probability reaches $R_{demo}(x_L^*) = 0.9$, indicating that the demonstration test has a 90% probability of success. This outcome is attributed to the increased

information gained from a greater number of failures. On the other hand, when the actual reliability approaches the MIL-B target value (R_{true}=0.9), the demonstrated lower bound x_L* must be set higher. In such cases, the demonstrated probability R_{demo} decreases, and reconfiguration of the demonstration test becomes necessary.

2.3 Effect of thermal and external load on mechanical behaviour on CFRP/Aluminium hybrid joints

Takao Okada[1], Tomo Takeda[1], Hisashi Kumazawa[1],Toshiyuki Kasahara[2], Sho Miyashita[3], Koichi Yamada[3], Kasumi Nagao[3] and Yuichiro Aoki[1]

[1]Japan Aerospace Exploration Agency (JAXA), Tokyo, Japan

[2] Adecco Group Japan, Tokyo, Japan

[3]Japan Aerospace Exploration Agency (JAXA), Tokyo, Japan

In ICAF2015, JAXA and NRC presented the life distribution up to first linkup of adjacent fatigue cracks formed in the riveted Aluminum lap joint under constant amplitude fatigue load. The fatigue life up to 0.5mm crack formation was predicted by SWT equation and the life up to first linkup was predicted using in house code [1].

Currently, JAXA has been conducted the research to evaluate the fatigue life up to form a fatigue crack in a metal/composite hybrid joint. Thermal stress at high and low temperature is occurred in metal/composite hybrid joints due to the difference of coefficient of thermal expansion between metal and composite materials. In ICAF2023, JAXA presents the experimental and numerical results for metal/composite hybrid joint under thermal cycles [2].

In this study, the mechanically fastened hybrid joint specimens composed of two aluminum plates and a composite plate are prepared. Most of the dimensions of the hybrid joint are same as those evaluated in previous research. The cyclic thermal and external loads are simultaneously applied to the hybrid joint and stress and strain on the aluminum plate are evaluated experimentally and numerically. From the behavior of the elastic strain, which is the total strain minus the thermal strain, it is shown that when thermal load and external load are coupled, the hysteresis loop becomes larger than when only the external load is repeatedly applied. In addition, it is shown that the strain and stress around the fastener holes in the top row through the load direction are high, and this could be a critical area for fatigue failure.

[1] T. Okada, M. Liao, S. Machida, G. Li and G. Renaud, WFD evaluation of riveted lap joint, proceedings of the 28th ICAF symposium, Helsinki, 2015.

[2] T. Okada, H. Kumazawa, T. Toyosawa, T. Takeda, T. Kasahara, K. Yamada, K. Nagao, Y. Aoki and H. Shoji, Research for thermal load and procedure to predict fatigue life up to form a fatigue crack on CFRP/Aluminum hybrid joints, proceedings of the 31st ICAF symposium, Delft, 2023.

3. FATIGUE AND FAILURE IN COMPOSITE MATERIALS AND COMPONENT

3.1 Ply Curving Termination for Improving Fatigue Characteristics of Composite Ply Drop-Off

S. Minakuchi[1]*, T. Yoshida

[1]The University of Tokyo, Tokyo, Japan

* tminakuchi@g.ecc.u-tokyo.ac.jp

Ply drop-off is a weak point of a tapered composite laminate, where stress concentration occurs and delamination initiates. By suppressing delamination from the ply drop-off, more optimized structural design and further weight reduction are possible. The authors' research group has been proposing Ply Curving Termination (PCT), which locally changes the fiber direction at the edge of the dropped ply (Fig. 3.1.1), to suppress delamination from the ply edge [1]. This study conducted tensile fatigue tests using asymmetric taper configuration. Damage initiation, delamination propagation, and final failure were evaluated in detail by changing the PCT fiber angle (Fig. 3.1.1) and loading level. The results confirmed that large PCT angles are effective in improving the fatigue properties of tapered laminates and that controlling the location of initial damage is necessary to maximize the effectiveness of PCT (Fig. 3.1.2). Based on the findings, an effective design guideline for tapered laminates with PCT can be discussed.

[1] Minakuchi, S., & Takeda, N. (2019). Ply curving termination to suppress delamination in composite ply drop-off. In International Committee on Aeronautical Fatigue (ICAF) (pp. 124-132). Cham: Springer International Publishing.

3.2 Effect of Interface Microstructure on Interlaminar Fracture Toughness in Dissimilar Joints of Thermoplastic CFRP and Aluminum Alloys

Atsushi Hosoi[1]

[1] Waseda University

Thermoplastic carbon fiber reinforced plastics (CFRPs) have excellent heat resistance and recyclability. However, some thermoplastics have poor adhesion due to their chemical stability. In particular, it is important to develop a technology for dissimilar bonding between thermoplastic CFRP and metals, which have high bonding strength and toughness. However, it is generally known that there is a trade-off between bonding strength and toughness with respect to adhesive thickness. The author fabricated nanostructures on the surface of aluminum alloys and bonded them to thermoplastic CFRP laminates. Both the bonding strength and toughness of the materials were improved by the nanostructures. Numerous fluffing of the resin was observed on the fracture surface, which is assumed to be a contributing factor, but the mechanism by which the nanostructure at the interface improves fracture toughness is not well understood. In this study, the crack tip element method is extended to evaluate the effect of bridging on crack propagation at dissimilar material interfaces.

The crack tip element method was used to derive the energy release rate associated with crack propagation at the interface of dissimilar materials. In this study, the energy release rate associated with interfacial crack propagation was derived by considering the bridging that occurs behind the crack tip. Figure 3.2.1 shows the proposed model considered in this study, where N, Q, and M represent axial force, transverse shear force, and bending moment, respectively. The subscripts 1 and 2 indicate the different types of materials. (x) indicates the physical quantity at distance x from the crack tip. The subscript T indicates the sum of materials 1 and 2. Figure 3.2.2 (a) shows bridging behind a crack tip and Figure 3.2.2 (b) shows the free body diagram at the crack tip. The subscript c represents the interfacial force acting in front of the crack tip. The subscript $i0$ (i = 1, 2) indicates the posterior direction of the crack.

Plain woven thermoplastic CFRP laminates with polyamide 6 matrix resin and aluminum alloy A5052 were used as test materials. The stacking sequence of the laminate was $[(0/90)_9]$. The thickness of both thermoplastic CFRP and aluminum alloy was 2 mm, respectively. Nanostructures were fabricated on aluminum alloy surfaces by two-step processes of anodizing and etching. In addition, to improve the bonding of aluminum alloy to the matrix resin of thermoplastic CFRP, a silane coupling agent was treated to the surface of an aluminum alloy. The double cantilever beam (DCB) tests were performed according to JIS K 7086. In the DCB test results, the fracture toughness of the specimen without nanostructure interface was G_c = 0.380 kJ/m^2 and that of the specimen with nanostructure interface was G_c = 0.984 kJ /m. Figure 3 shows the R-curve of the specimen calculated using the proposed model considering micro-bridging behind the crack tip. The critical energy release rate at crack initiation without micro-bridging was G_0 = 0.371 kJ/m^2. The steady-state energy release rate with micro-bridging was G_{ss} = 1.068 kJ/m^2. These results are in good agreement with the experimental results.

The energy release rate associated with crack propagation at the bonding interface was derived by considering bridging behind the crack tip in dissimilar materials. The R-curve associated with crack propagation was evaluated using the proposed model. The analytical results showed good agreement with the experimental results. It is suggested that micro-bridging at the interface may have higher strength due to the size effect and may increase resistance to crack propagation.

3.3 Numerical analysis of fatigue evolution of laminated composites using cohesive zone model and extended finite element method

Rong-Can Hong[1], Ryo Higuchi[1], Xin Lu[1], Tomohiro Yokozeki[1]

[1]The University of Tokyo, Tokyo, Japan

A numerical method for fatigue accumulation of in laminated composites is developed in this paper. Extended finite element method (XFEM) and cohesive element are integrated into a numerical program for modelling intralaminar matrix cracking and delamination in composite laminates, respectively. A damage-mechanics-based fatigue model is also introduced into the numerical scheme. Pure modes fatigue tests are used for the identification of fatigue parameters. The simulation of open hole tensile test is then performed to investigate the fatigue behaviors of composite laminates. The numerical damage distribution aligns with

prior test records, while the predicted fatigue life is consistent with the referenced data. The fast crack propagation observed in the reference is also captured. This study demonstrates that the proposed numerical method can predict the fatigue initiation and evolution of multi-cracks under mixed mode loading, introducing a convenient approach to effectively simulate multiple fatigue cracks in composite laminates.

3.4 Experimental study of intrinsically conductive resin as a functional repair for CFRP laminates against simulated lightning strike

Tomohiro Yokozeki[1], Teruya Goto[2], Tatsuhiro Takahashi[2], Takao Okada[3], Hiromitsu Miyaki[3] and Shintaro Kamiyama[3]

Yu Zhou[1], Tomohiro Yokozeki[1]*, Shintaro Kamiyama[2], Takao Okada[2]

[1]The university of Tokyo, Tokyo, Japan

[2]Japan Aerospace Exploration Agency, Tokyo, Japan

*E-mail address: yokozeki@aastr.t.u-tokyo.ac.jp

Non-metallic coatings offer promising applications for protecting carbon fiber-reinforced plastics (CFRP) from lightning, preserving the strengths of epoxy-based composites without galvanic corrosion concerns. This study explores the electrically conductive polyaniline-based resin's dual role: as protective coating and repair solution for traditional metal layer/CFRP lightning strike protection (LSP). We evaluated the impact of coating thickness and surface roughness on lightning resistance. The results show that a 0.4 mm thick coating with a 400-grit pretreatment demonstrated minimal damage after a 40 kA simulated lightning strike, maintaining 96 % residual strength. Furthermore, we investigated the resin's capability as a functional repair for the conventional LSP system. When employed to repair the damaged CFRP panel, the resin showcased its efficacy by preserving more than 95 % of the system's residual strength even after a subsequent lightning strike. These results indicate the proposed conductive resin could be a new practical repair approach for lightning strike damage to the conventional metal layer.

4 NON DESTRUCTIVE INSPECTION

4.1 Characterization of delaminations in CFRP laminates through data fusion with ultrasonic Lamb waves and thermography

Lea Lecointre[1], Tomohiro Yokozeki[1*], Naoki Hosoya[2], Shintaro Kamiyama[3] and Shin-ichi Takeda[3]

[1] The university of Tokyo, Tokyo, Japan

[2] Shibaura Institute of Technology, Tokyo, Japan

[3] Japan Aerospace Exploration Agency, Tokyo, Japan

*E-mail address: yokozeki@aastr.t.u-tokyo.ac.jp

Every Non-Destructive Testing (NDT) technique has some advantages and some limitations. To overcome these, investigations on how to improve the advantages and overcome the limitations of each technique are often reported. Another approach is the fusion of quantitative results extracted from different techniques. In this study, thermal diffusivities are extracted from InfraRed Thermographic inspection and Root Mean Square (RMS) signal values are extracted from Lamb Waves inspection in various structures of CFRP samples including damaged zones. The results shown that the fusion of thermal diffusivity and RMS values allowed us to obtain a better characterization of damaged zones, particularly for stiffened samples and for samples damaged from artificial lightning strike test. These results allow us to highlight very interesting perspectives for a new philosophy around NDT.

5. MISCELLANEOUS

5.1 Clarifying the mechanisms of edge glow generation in CFRP laminates exposed to lightning currents

Shintaro Kamiyama[1], Takao Okada[1], Yoshiyasu Hirano[1], Takeo Sonehara[2], Hiromitsu Miyaki[1], Toshio Ogasawara[3]

[1] Japan Aerospace Exploration Agency, Tokyo, Japan

[2] Shoden Corporation, Tokyo, Japan

[3] Tokyo University of Agriculture and Technology, Tokyo, Japan

Carbon fiber-reinforced plastic (CFRP) has been widely used in primary aircraft structures because of its high specific strength and stiffness. One of the most serious hazards to aircraft structures, especially those made of CFRP, is lightning strikes during operation [1]. When an aircraft is struck by lightning, inspection, and repair must be performed, which leads to reduced operational efficiency. Edge glow occurs at the edge of a CFRP when a lightning current passes through it. Edge glow may be an ignition risk in a composite fuel tank [2]. Therefore, it must be understood and mitigated or eliminated to certify the safety of aircraft. The cut edge of the CFRP is often sealed with a polysulfide coating, or elastomeric caps adhesively bonded to it. Research on edge glow has been primarily performed by aircraft manufactures, and few studies have been published in academic journals. Fundamental process of the generation and propagation of the edge glow has not been elucidated.

Unidirectional prepreg tapes of carbon fiber/toughened epoxy (IMS60/#133, Teijin) were used for conduction tests. Prepreg tapes were laminated in three different configurations: $[0]_{16}$, $[0/90]_{4s}$, $[45/0/-45/90]_{2s}$ and cured in an autoclave at 180°C for 2 h. An impulse current of 12 kA with positive polarity, in accordance with the component A waveform defined in SAE ARP 5412 [3] which simulates the initial stroke of lightning, was applied to each specimen (Fig. 5.1.1). To clarify the edge glow mechanisms, impulse current was applied in atmospheric environment and silicone oil bath.

Fig. 5.1.2 shows typical images captured using a high-speed camera. The left side of Fig. 5.1.2(a) shows the observation area before the test. Owing to the constraints of the testing setup, the left side of the specimen was observed. In the case of unidirectional laminate UD0 and cross-ply laminate CP, nothing was observed in air and silicone oil (Fig. 5.1.2(a)). However, for the QI laminate, an edge glow is observed at the edge of the specimen in air (Fig. 5.1.12(b)). The edge glow occurred approximately 4 μs after the application of the impulse current. Fig. 5.1.2(c) shows the edge glow phenomenon of the QI in silicone oil. The edge glow was suppressed in silicone oil because the emission intensity of the edge glow was much lower than that in air. The edge glow was more suppressed in silicone oil than in air. The dielectric strength of the silicone oil used in this study was approximately 69 kV/2.5 mm (25°C, water content of 75 ppm), which was an order of magnitude greater than that of air. These experimental results indicate that the edge glow is caused by the

breakdown of the insulation of the testing environment owing to the large potential difference of several hundred volts between the layers.

[1] Chemartin L, Lalande P, Peyrou B, Chazottes A, Elias PQ, Delalondre C et al. Direct Effects of Lightning on Aircraft Structure: Analysis of the Thermal, Electrical and Mechanical Constraints. Aerosp Lab 2012;5:1–15.
[2] SAE ARP 6205, Transport Airplane Fuel System Lightning Protection, 2023.
[3] SAE ARP5412B, Aircraft Lightning Environment and Related Test Waveforms, 2013.

5.2 Aircraft Accident and Serious Incident Investigation

Koichi Minato
Japan Transport Safety Board (JTSB), Tokyo, Japan

(1) Statistics related to the accident and serious incidents investigation

The number of accidents and serious incidents which JTSB investigated in the past two years are shown in Tables 5.2.1 and 5.2.2 of a total of 66 occurrences, large airplanes accidents and serious incidents were 17, small airplanes were 20 and rotorcraft were 18. Gliders, ULPs (ultra-light planes) and others were remaining 11 occurrences.

(2) Fatigue failure related accident

1) Summary of the accident

On Sunday, August 1, 2021, at about 11:33 Japan Standard Time (JST: UTC + 9 hours, all times are indicated in JST on a 24-hour clock), a privately owned Piper PA-46-350P, JA4077, sustained substantial damage when landing at Sendai Airport during the landing roll because it tilted forward with the nose down, the propellers and the lower forward fuselage contacting with the runway surface (Figure 5.2.1).

A total of two persons on board the aircraft, including a captain and a passenger, and there were no injuries.

2) Damage to the aircraft

As the retractable NLG collapsed in the retracted direction, the aircraft tilted forward, the lower forward fuselage made contact with the runway surface, which caused the tips of three propellers to be damaged, and the NLG strut and door, and part of the skin of the lower front fuselage to be damaged and deformed. In addition, in the forward fuselage, part of the engine mount was broken and deformed.

The engine mount of the aircraft is a base-like part to fix not only the engine but also the NLG strut and NLG actuator. The NLG actuator is bolted being sandwiched from the left and right sides via the actuator attachment feet, which is part of the engine mount. The engine mount of the aircraft was found

deformed where the right actuator attachment foot area was fractured, only the left foot was supporting the actuator, and the tip of actuator had been found hit the firewall, deforming part of the firewall. Removal and examination of the Fractured Portion A (Figure 5.2.2) revealed partial corrosion on the fracture surface and blisters had occurred on the back side of the welded part (Figure 5.2.3).

3) Past similar incidents or accidents and responses taken by the design and manufacturing company

In the past, there had frequently occurred the incidents or accidents involving same model airplanes and its similar models that resulted from cracks and fractures in the actuator attachment areas with the same shape as in the aircraft. In response to the failure cases, the design and manufacturing company issued Service Bulletin (SB) 1103 on April 22, 2002 (the latest version at the time of the accident was issued on September 1, 2015 as the SB 1103F), to instruct fluorescent penetrant inspection at each 100 hours time in service for the actuator attachment area. The company analyzes that the cracking in the actuator attachment foot areas usually occurs on the outer surface of cylindrical foot along the weld joining due to a one-time overload event such as a hard landing, and propagates through according to the repetitive landing cycles, slowly leading to fatigue cracking and eventually to fractures. In addition, the company also express their opinion that cracking can take a long period of time from occurrence leading to fracture, during which corrosion may occur on the fractured surface of cracks where the metal surface is exposed. The company has redesigned the actuator attachment foot and currently provides the redesigned engine mount that each attachment foot is a one-piece machined part. The airplanes whose engine mounts were replaced with the redesigned ones can eliminate the fluorescent penetrant inspection at each 100 hours time in service.

4) Maintenance history of the aircraft

On November 23, 2020, the aircraft underwent a 100hr periodic inspection (equivalent to an annual inspection), including an inspection of the engine mount actuator attachment areas during the maintenance work for airworthiness certification inspection. According to the mechanics who performed the relevant maintenance work, the visual inspection of the actuator attachment areas revealed no anomalies such as cracks, therefore they did not perform the fluorescent penetrant inspection instructed by SB 1103F. In addition, it could not be confirmed whether anticorrosive measures were taken periodically in the past maintenance work.

5) Analysis of Findings

The JTSB concludes that it is certain that because the NLG collapsed in the retracted direction during the landing roll, the aircraft tilted forward, the propellers and the lower forward fuselage contacting with the runway surface to be damaged as well as the actuator in the extended position hit the firewall, deforming it. From the fact that the NLG of the aircraft had collapsed in the retracted direction with the actuator in extended and down-locked position, it is certain that during the landing roll, fractured was the right one of the left and right actuator attachment feet fixing the actuator that had retained the NLG in the down-locked position, thus loads from the NLG concentrated on the left attachment foot, which deformed

the engine mount that could no longer support the actuator, leading to the collapse of the NLG in the retracted direction.

The JTSB concludes that it is certain that as partial corrosion occurred on the fracture surface of the right actuator attachment foot, the cracking had occurred before this accident occurred and it had progressed over the repeated flights, leading to the fractures. The analysis of the fractured surface revealed that the right actuator attachemt foot fractured, because blisters around the inner surface of the cylindrical foot along the weld joining occurred due to corrosion, it is probable that in the blister part, non-through cracks originating from the inner surface were formed, developed into through cracks later, and progressed to its end further.

The JTSB concludes that cracks originating from the inner surface of the right actuator attachment foot more likely had occurred in the past due to impacts at the time of landings and others. As the corrosion occurred on the inner surface of the right actuator attachment foot, the corroded part was likely weakened, which possibly contributed to the cracks originating on the inner surface. However, as corrosion occurred on the fracture surface, striation (Striped traces indicating fatigue failure due to repetitive stress) was unable to be observed with a scanning electron microscope, it was unable to estimate the progressing speed of the cracks. Accordingly, it was unable to estimate when the cracks originating from the blister formed. Besides, component analysis was conducted on the sample taken from the right actuator attachment foot with an Energy Dispersive X-ray Spectroscopy to calculate the proportion of each element in the base metal and welded part using the sum of carbon, oxygen, silicon, chromium, and iron as 100%. As a result, it was confirmed that the proportion of chromium, which contributes to the corrosion resistance of iron steel, was 0.90 to 1.09 % in the base metal, but 0.49 to 0.73 % in part of the welded portion, and there was a deficiency in chromium. Chromium-deficient area more likely had lower corrosion resistance than that in the base metal due to their lower chromium content, which likely caused corrosion to occur and blisters to be formed in the welded part. Chromium was deficient in part of the welded portion was probably because the precipitation of the chromium contained in alloy was generated by influences of the heat temperature and hours at the time of welding. Regarding the corrosion that occurred on the inner surface of the welded part, it is probably that in addition to the corrosion resistance property in the welded part, several factors contributed to such as the custodial environment and conditions of the aircraft, characteristics of cylindrical shape whose inner surface is considered to be prone to residual moisture due to condensation and others. Therefore, it was unable to determine when and how the corrosion occurred. Japan has a humid climate with a lot of precipitation, making it an environment with a high risk of corrosion. And when using the airport located in coastal areas as its homebase as in the case of the aircraft, it is susceptible to the influence of sea breeze, therefore, careful attention should be paid to corrosion.

In addition, according to the analysis of the company, in the past similar case, the cracks of actuator attachment area occurred on the exterior of the cylindrical foot along the weld joining. Accordingly, this accident of the aircraft where the cracks more likely occurred originating from the inner surface is probably a unique case.

ACKNOWLEDGEMENT

The editor appreciated the members of the ICAF national committee of Japan Society for Aeronautical and Space Sciences and other participants in the committee, for their contribution in preparation of this national review and contributing discussion in the committee.

Table 5.2.1 Number of accident by type of aircraft

Aircraft Year	Large Airplane	Small Airplane	Rotorcraft	Glider, ULP or others	Total
2023	4	5	5	3	17
2024	7	4	4	4	19

Table 5.2.1 Number of serious incident by type of aircraft

Aircraft Year	Large Airplane	Small Airplane	Rotorcraft	Glider, ULP or others	Total
2023	2	6	4	2	14
2024	4	5	5	2	16

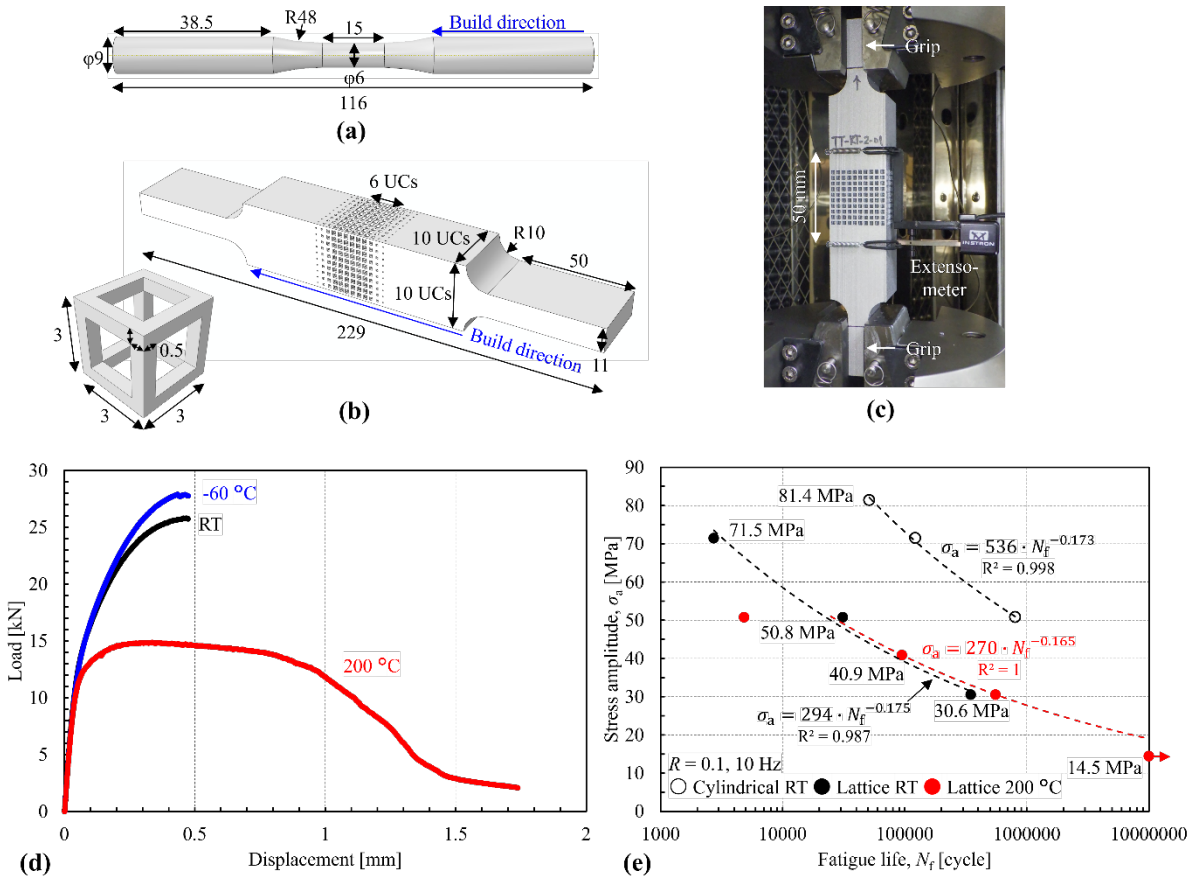

Figure 2.1.1 (a) Cylindrical specimen, (b) lattice specimen, (c) test set-up of lattice specimen, (d) load-displacement curves of lattice specimens in static tensile tests, (e) S-N diagram in fatigue tests.

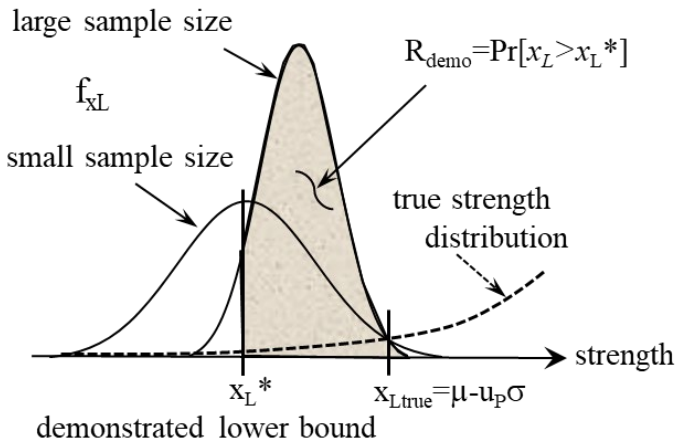

Figure 2.2.1 Demonstrated probability: R_{demo} and distribution of torelance limit x_L : f_{xL}

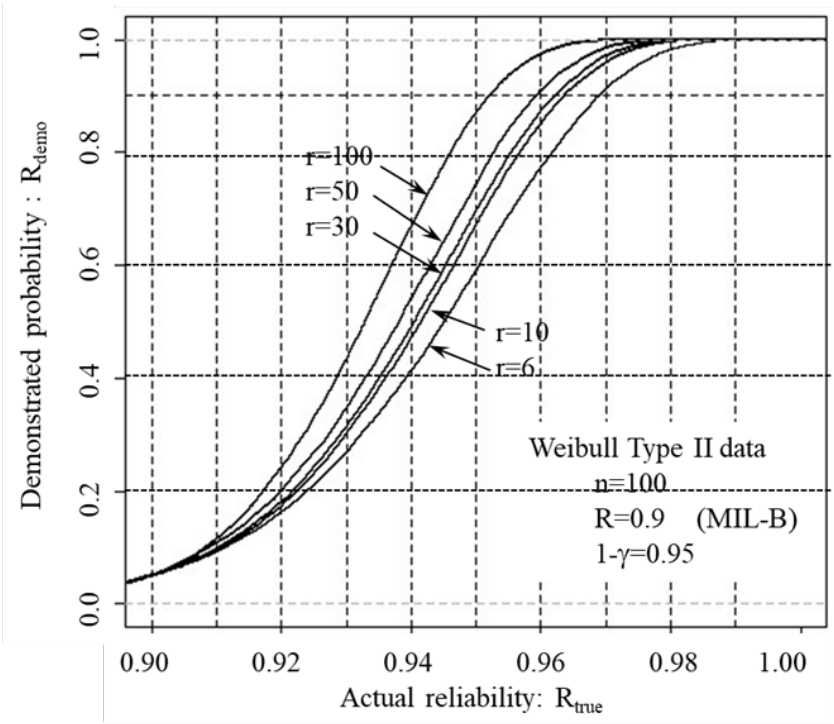

Figure 2.2.2 Demonstrated probability for Weibull Type II data

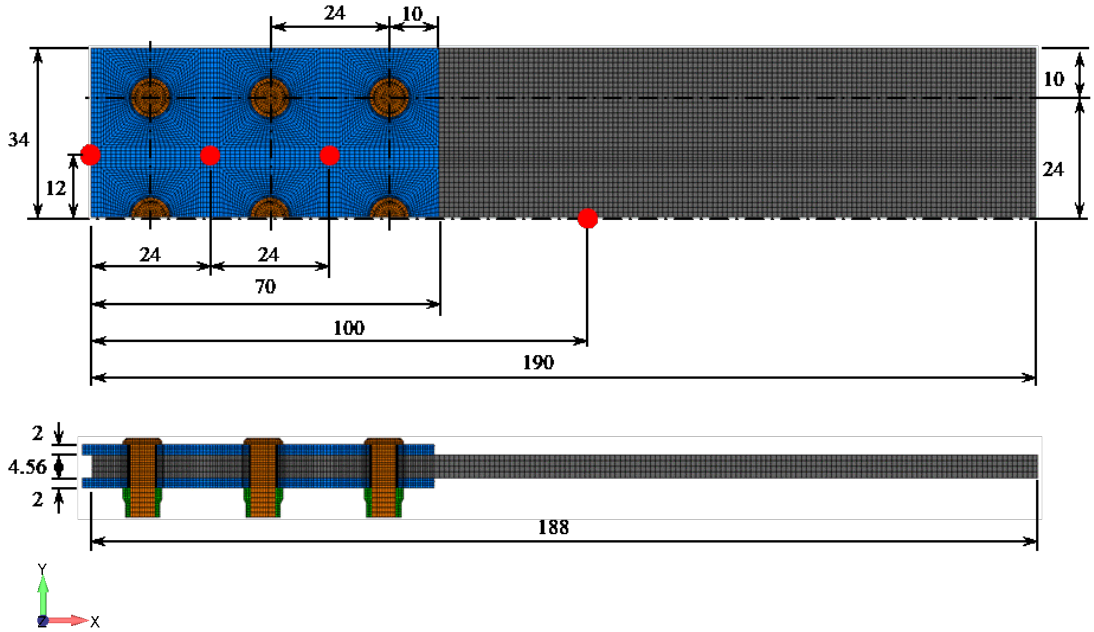

Figure 2.3.1 FEM model of the hybrid joint

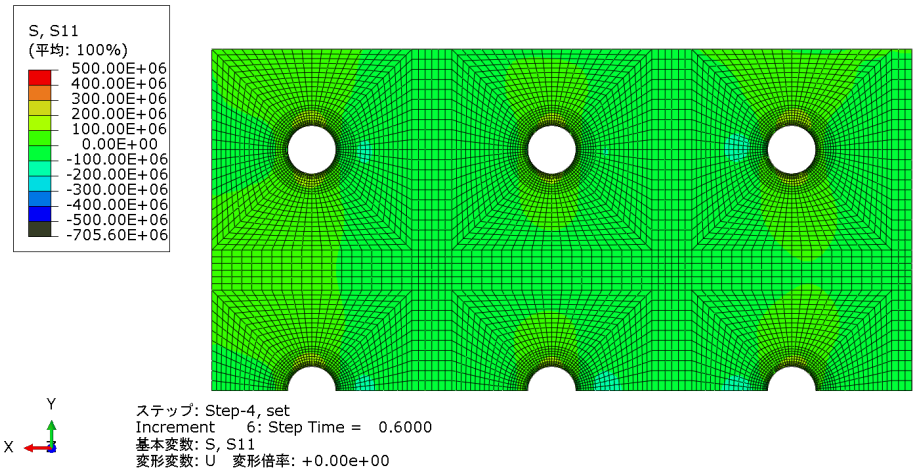

(a) -55 deg C, 47 kN

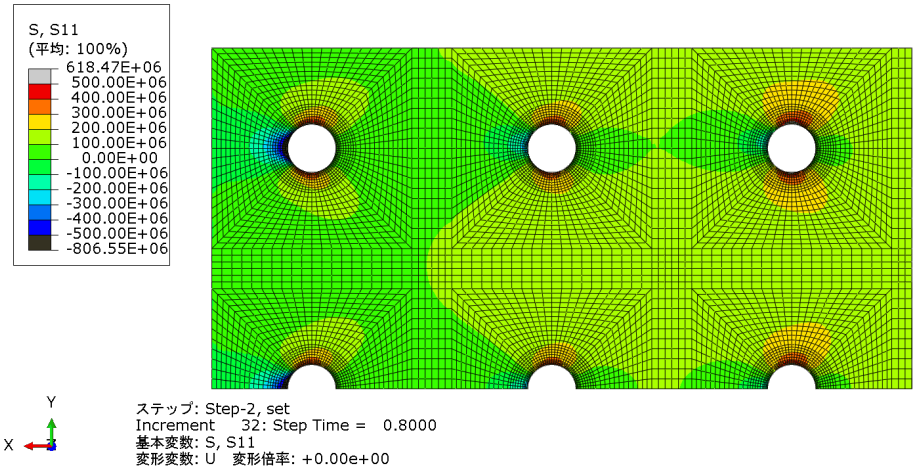

(b) 85 deg C, 0 kN

Figure 2.3.2 S11 (Sxx) contour at z=2.28mm on Aluminum plate

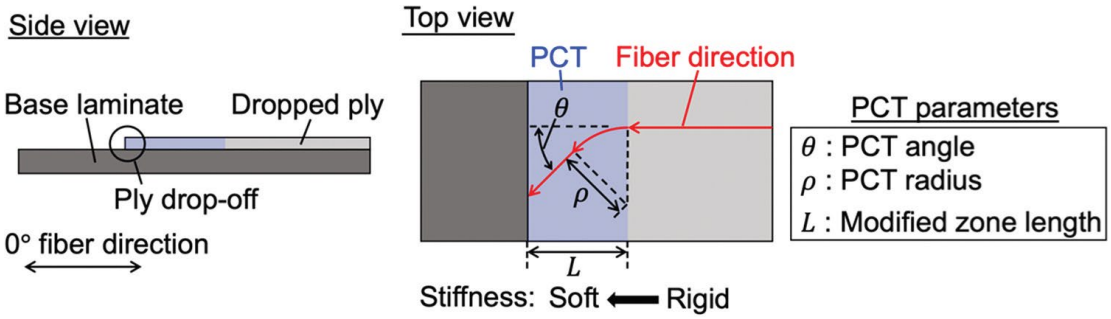

Fig.3.1.1 Tapered laminate with PCT and definition of PCT parameters.

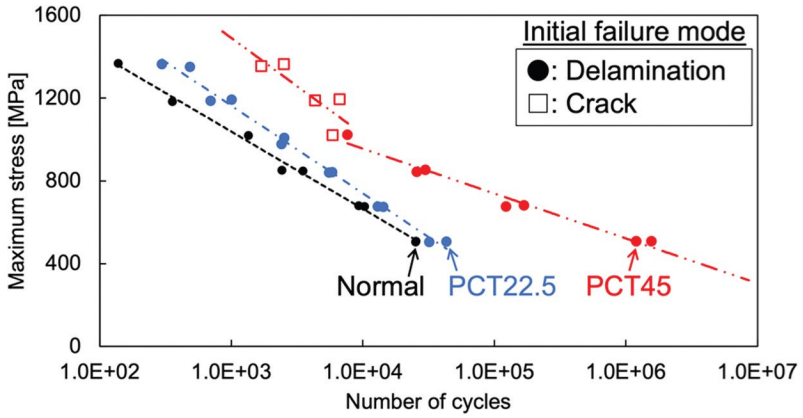

Fig. 3.1.2 Number of cycles to final failure. PCT45, with the largest PCT angle of 45°, has the largest failure cycle, and delamination from the ply edge is the initial damage that maximizes the effectiveness of PCT.

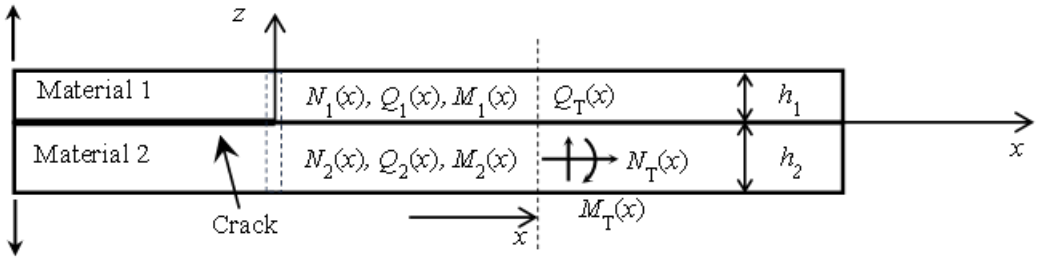

Figure 3.2.1 A bi-layer model with cracks under DCB test.

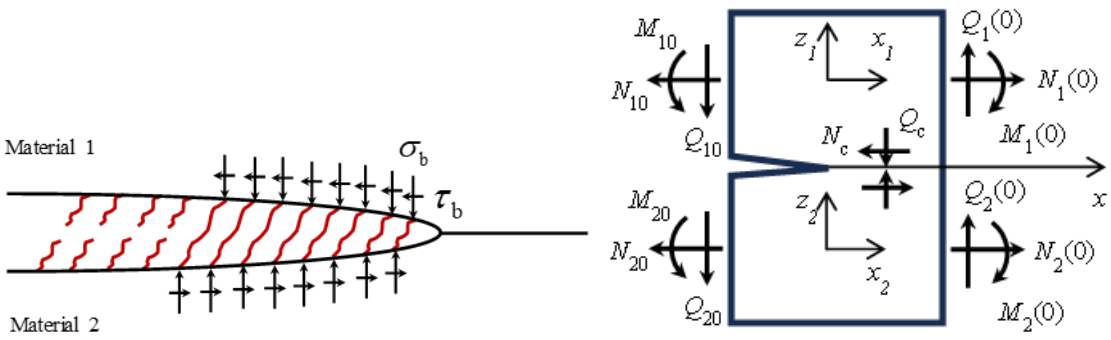

Figure 3.2.2 Mechanical state near crack tip:
(a) Bridging behind a crack tip; (b) Free body diagram at crack tip.

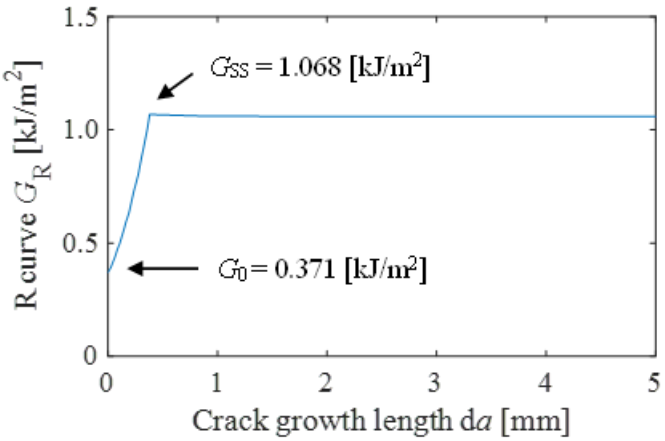

Figure 3.2.3 Predicted R-curve of the DCB specimen with micro-bridging behind the crack tip.

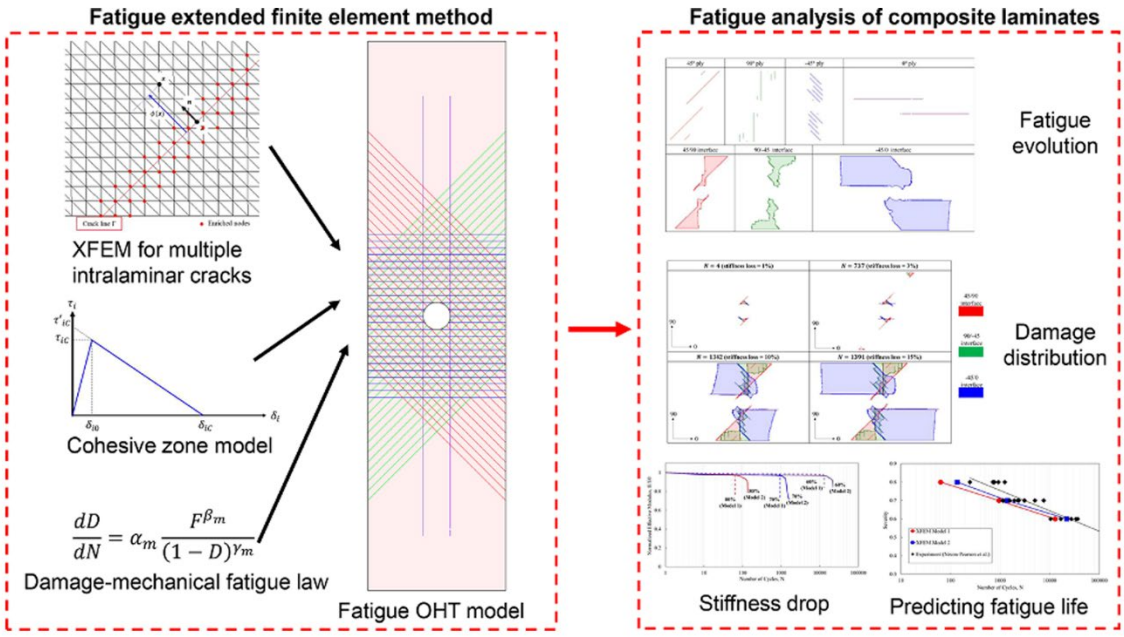

Figure 3.3.1: Transformed Coulomb-Mohr Model

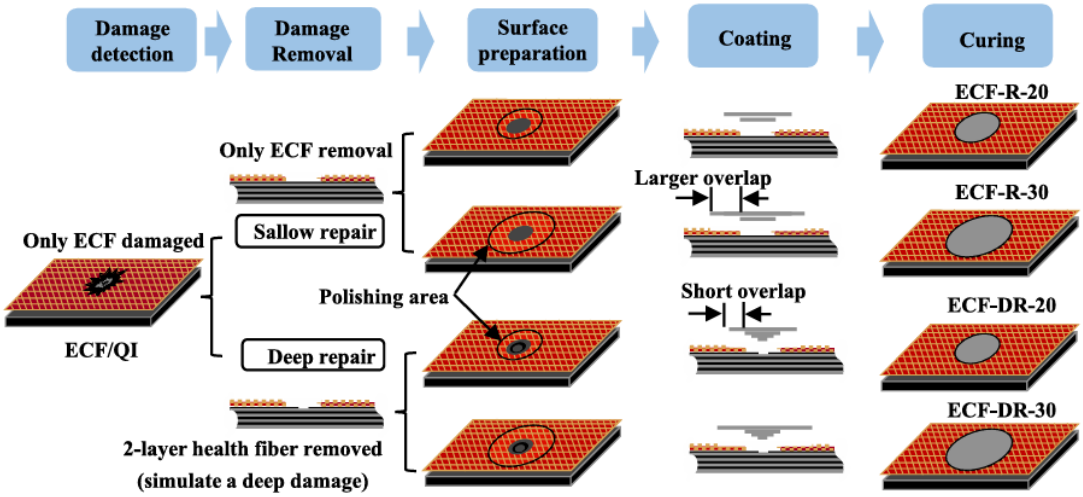

Figure 3.4.1: Repair process for CFRP

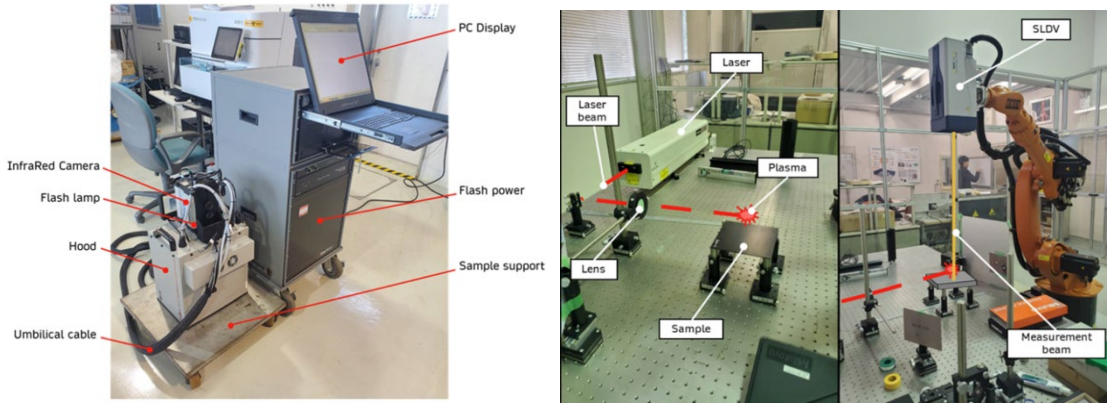

Figure 4.1.1 Test setup

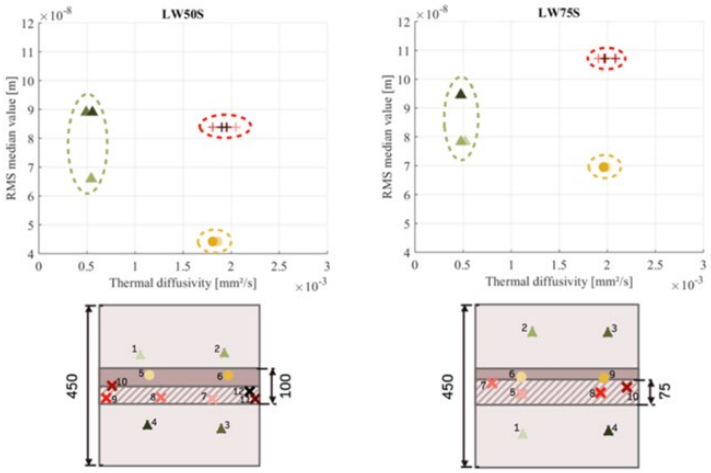

Figure 4.1.2 Test results

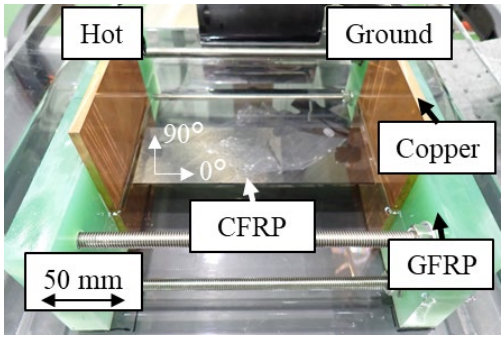

Figure 5.1.1 Experimental setup.

(a) CP_air

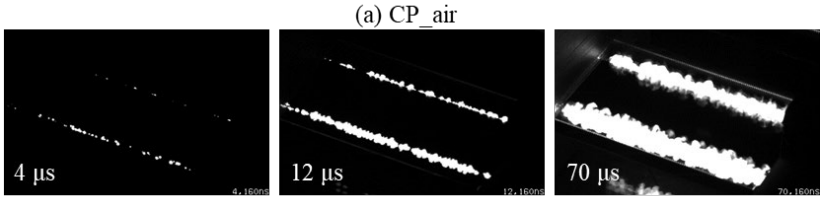

(b) QI_air

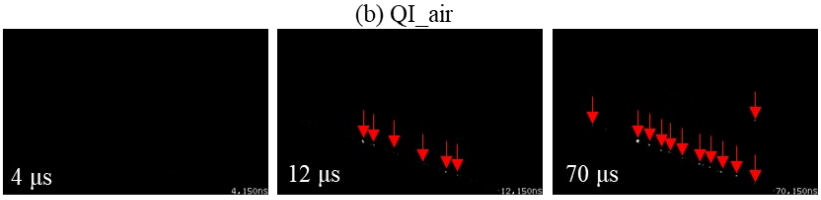

(c) QI_oil

Figure 5.1.2 Edge glow captured by high-speed camera. Red arrows indicate the location of the edge glow.

Figure 5.2.1 The aircraft at time of accident

Figure 5.2.2 Fractured portion A (left: actuator side, right: engine mount side)

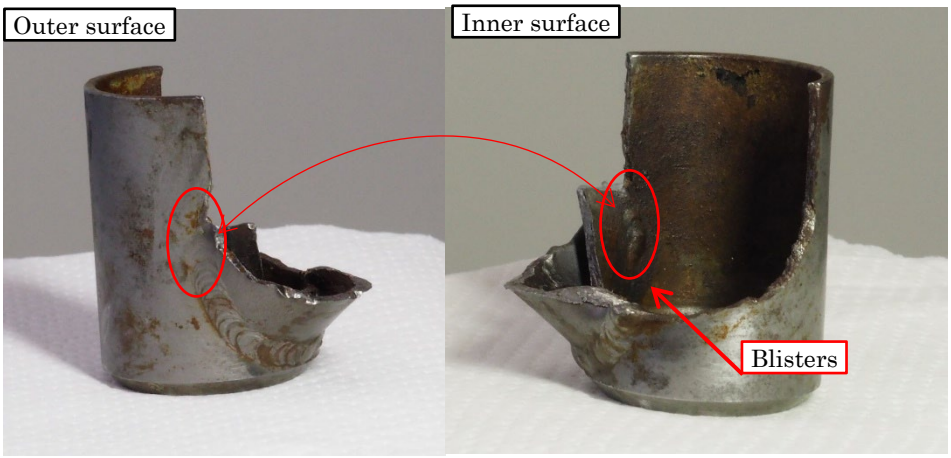

Figure 5.2.3 Blisters on fractured portion A